J. Fluid Mech. (1995), *vol.* 304, *pp.* 119–141

Merging flows in an arterial confluence: the vertebro-basilar junction

By J. RAVENSBERGEN[1], J. K. B. KRIJGER[1], B. HILLEN[1] AND H. W. HOOGSTRATEN[2]

[1]Department of Functional Anatomy, Utrecht University, The Netherlands

[2]Department of Mathematics, University of Groningen, The Netherlands

(Received 9 March 1994 and in revised form 22 May 1995)

The basilar artery is one of the three vessels providing the blood supply to the human brain. It arises from the confluence of the two vertebral arteries. In fact, it is the only artery of this size in the human body arising from a confluence instead of a bifurcation. Earlier work, concerning flow computations in simplified models of the basilar artery, has demonstrated that a junction causes distinctive flow phenomena. This paper presents three-dimensional finite-element computations of steady viscous flow in a rigid symmetrical junction geometry representing the anatomical situation in a more realistic way. The geometry consists of two round tubes merging into a single round outlet tube. The Reynolds number for the basilar artery ranges from 200 to 600, and both symmetrical and asymmetrical inflow from the two inlet tubes has been considered.

Just downstream of the confluence a 'double hump' axial velocity profile is found. In the transition zone the flow pattern appears to have a complicated structure. In the symmetrical case the axial velocity profile shows a sharp central ridge, whereas in the asymmetrical case the highest 'hump' crosses the centreline of the tube. The flow has a highly three-dimensional character with secondary velocities easily exceeding 25% of the mean axial flow velocity. The secondary flow pattern consists of four vortices. Under all simulated flow conditions, the inlet length turns out to be much larger than the average length of the human basilar artery.

To validate the computational model, a comparison is made between numerical and experimental results for a junction geometry consisting of tubes with a rectangular cross-section. The experiments have been performed in a Perspex model with laser Doppler velocimetry and dye injection techniques. Good agreement between experimental and computational results is found. Moreover, all essential flow phenomena turn out to be quite similar to those obtained for the circular tube geometry.

1. Introduction

Blood flow in large arteries has been a subject of interest for many authors (McDonald 1974; Caro *et al.* 1978; Pedley 1980). During the last decade both numerical and experimental methods were applied to investigate the arterial flow phenomena in increased detail. The carotid artery bifurcation, the aortic bifurcation and the coronary arteries have attracted most attention, mainly because these arteries are often affected with atherosclerosis, by far the most common process responsible for cardiovascular and cerebrovascular diseases.

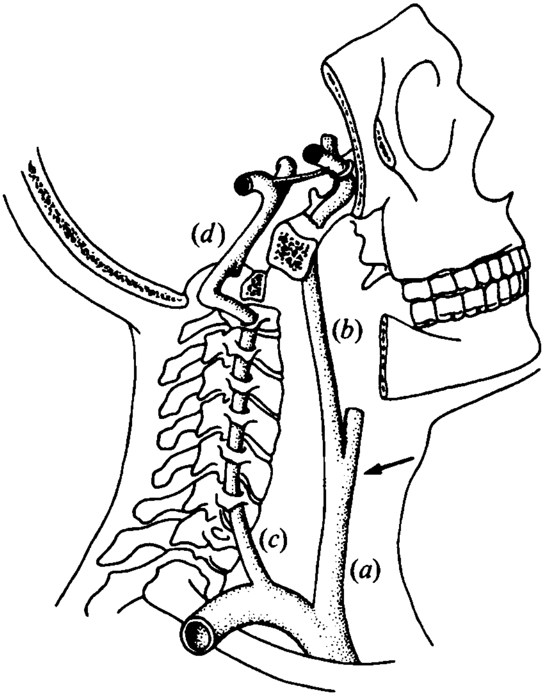

FIGURE 1. Diagram of the arteries of the brain in relation to the skeleton. (*a*) Right common carotid artery. (*b*) Right internal carotid artery (*arrow*: carotid bifurcation). (*c*) Right vertebral artery. (*d*) Basilar artery.

Essentially, the arterial tree is a branching system. The basilar artery is the largest artery arising from a confluence. It has a length of approximately 35 mm and an internal diameter of 3–4 mm. Together with the two internal carotid arteries, the basilar artery is responsible for the blood supply to the human brain. Figure 1 shows a diagram of these arteries in relation to the skeleton. At the entrance of the basilar artery the flows from the two vertebral arteries merge. The basilar artery and the internal carotid arteries discharge into the circle of Willis, an arterial network at the base of the brain. From this circle of Willis, six cerebral arteries distribute the blood to various parts of the brain.

Up to now, little attention has been paid to flow phenomena in an arterial confluence. One of the first studies concerning the flow in the basilar artery was made by McDonald & Potter (1951). In an elegant experiment, they exposed the vertebral arteries and the basilar artery of anaesthetized rabbits, introduced ink in one of the vertebral arteries and made a film of this *in vivo* flow visualization. They noted that, under symmetrical flow conditions, the ink remained on its own side and drained into the branches of the basilar artery on that side exclusively. Schroter & Sudlow (1969) did flow experiments in a symmetric model of a human bronchial bifurcation. They measured velocity profiles with hot-wire anemometry and visualized the structure of the secondary velocity field with smoke during inspiratory and expiratory air flow. The latter is comparable with our flow conditions. In those days only axial flow velocities could be measured and no sufficiently accurate numerical computations could be performed. Therefore, no quantitative information on the strength of the secondary flow field, nor on the distribution of the wall shear stress and the pressure could be obtained. Some laser Doppler anemometer measurements in a vertebro-basilar junction model were performed by Hayashi *et al.* (1992). However, the spatial resolution as well as the intervals along the basilar part of the model were insufficient to obtain detailed quantitative information about the flow patterns in the basilar artery. To the authors' knowledge, the flow in models of the basilar artery was computed for the first time only recently (Krijger, Hillen & Hoogstraten 1989, 1991; Krijger *et al.* 1990). They computed the flow velocities in simplified, mostly two-dimensional models of the vertebro-basilar junction. This work demonstrated that a junction causes distinctive flow phenomena. Subsequent computations of flow velocities in three-dimensional junction models consisting of channels of rectangular cross-section have shown that, analogous to the branching flow in a bifurcation, the merging flow in a confluence is characterized by the presence of a strong secondary flow field (Krijger *et al.* 1992).

The aim of the present study is to obtain a proper description of the flow phenomena in a geometrically realistic model of the basilar artery. The dimensions of the model are based on a morphological study of 85 human vertebro-basilar specimens originating from formalin-fixed dissecting room material. Although a wide variation of most geometrical parameters was found, it is impossible to study the influences of all of them at the same time. So we considered a standardized model geometry with equal diameters for both inlet channels, a biologically realistic ratio of inlet and outlet diameters, an average angle of confluence and a long and straight outlet channel without a bifurcation at the end, and studied the influence of different flow rates and inflow ratios. Furthermore, hemodynamical simplifications are used. Steady flow of a Newtonian fluid is considered in a rigid model, neglecting pulsatility, rheological blood characteristics and wall distensibility.

The computational model has been validated by hydrodynamical experiments in a Perspex model under various flow conditions using laser Doppler velocimetry. For this purpose, the definition of the geometry in the creation of both the numerical and the experimental model has to be very precise and the computational region and the Perspex model must be identical. Therefore, a model with rectangular channel cross-sections was chosen. A more qualitative validation is also performed by comparing the results of dye experiments with computed streamlines.

2. The computational model

The physiological situation has been simulated by computing steady flow of an incompressible Newtonian viscous fluid through a rigid junction model. The geometry and dimensions of this model are presented in figure 2. The model consists of two identical circular cylinders A and B (the inlet tubes, representing the vertebral arteries), connected with the circular cylinder D (the outlet tube, representing the basilar artery) by the junction region C. The axes of the cylinders lie in one plane and the geometry possesses two symmetry planes. The x, y, z-coordinate system has its origin at the junction apex and is defined as indicated in figure 2. The ratio between the total cross-sectional area of the two inlet tubes and the cross-sectional area of the outlet tube, the branching ratio, is equal to 1.2.

In the flow region extending from the two inflow planes to the cross-section $z = 25$ mm of the outlet tube the governing Navier–Stokes equations have been solved numerically by use of the the software package *Sepran* (Segal 1993), a finite-element programme that is able to compute accurately complicated three-dimensional flows. The finite-element method implemented in *Sepran* makes use of a Galerkin discretization approach which leads to a set of nonlinear algebraic equations (Cuvelier,

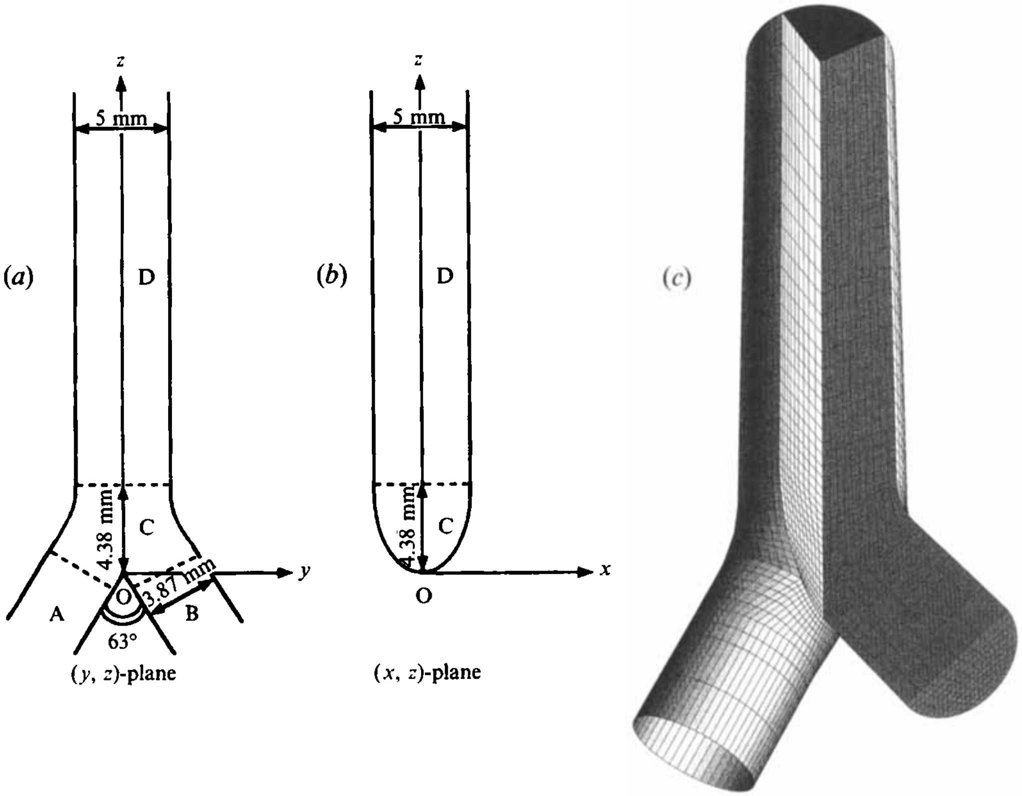

FIGURE 2. (*a*,*b*) Definition sketches. (*c*) Finite element mesh. Part of the mesh has been removed to show the finite-element discretization.

Segal & Van Steenhoven 1986; Van de Vosse *et al.* 1989). The discretized momentum equation becomes

$$\{\boldsymbol{S}+\boldsymbol{N}(\boldsymbol{u})\}\boldsymbol{u}+\boldsymbol{L}^T\boldsymbol{p}=\boldsymbol{b},$$

and the continuity equation in discretized form reads

$$\boldsymbol{L}\boldsymbol{u}=\boldsymbol{0}.$$

In these equations $\boldsymbol{u}$ denotes the column vector of n velocity unknowns in the nodal points for the velocity, $\boldsymbol{p}$ the column vector of m pressure unknowns in the nodal points for the pressure, $\boldsymbol{S}$ the $n\times n$ diffusion matrix, $\boldsymbol{N}(\boldsymbol{u})$ the $n\times n$ convection matrix, $\boldsymbol{L}$ the $m\times n$ divergence matrix and $\boldsymbol{b}$ the $n\times 1$ vector arising from the boundary conditions. This set of equations can be solved iteratively by solving at each step a linearized set. However, since a direct method is used for the solution of the linearized equations, this would result in a very time-consuming algorithm. The reason for this is that $\boldsymbol{p}$ does not occur in the continuity equation, which leads to a number of zero elements on the main diagonal of the coefficient matrix of the linearized equations, necessitating an expensive partial pivoting procedure. For that reason, a penalty function method has been implemented (Cuvelier *et al.* 1986) in which the continuity equation is replaced by

$$\boldsymbol{L}\boldsymbol{u}=\varepsilon\boldsymbol{M}\boldsymbol{p},$$

where ε is a very small penalty parameter and $\boldsymbol{M}$ is an $m \times m$ orthogonal projection matrix (the pressure matrix). The number of unknowns is now reduced from $n+m$ to n by elimination of $\boldsymbol{p}$ from the momentum equation, yielding a single equation for the vector $\boldsymbol{u}$:

$$\{\boldsymbol{S}+\boldsymbol{N}(\boldsymbol{u})\}\boldsymbol{u}+\varepsilon^{-1}\boldsymbol{L}^{T}\boldsymbol{M}^{-1}\boldsymbol{L}\boldsymbol{u}=\boldsymbol{b}.$$

This equation is conveniently solved by iteration. In each iteration step the linearized equation, obtained by use of the Newton–Raphson method, is solved by a direct method: asymmetric LU factorization without pivoting. Since the small value of the penalty parameter results in a poorly conditioned coefficient matrix, iterative solution methods are difficult to apply here.

The finite-element mesh is shown in figure 2(*c*). It is composed of 27-noded isoparametric hexahedral elements, each with 81 unknowns for the velocity and 4 for the pressure (Van de Vosse *et al.* 1989). The four pressure unknowns are the pressure itself and its three spatial derivatives, all of them defined at the centre of the element. The velocity components are approximated continuously by quadratic interpolation functions, whereas the pressure is interpolated linearly in each element and varies discontinuously over the element boundaries. The mesh has been constructed from previous meshes by gradual refinement in regions where wiggles in the numerical solution occurred until a smooth solution was obtained. Since wiggles were not suppressed artificially, a solution can usually be relied upon once the wiggles have been reduced. The smallest elements are located in the junction region C, where the most complicated flow phenomena occur.

In the case of symmetrical inflow from the two inlet tubes, the flow pattern possesses two symmetry planes, the (x,z)- and the (y,z)-plane, and in the case of asymmetrical inflow only one symmetry plane remains, the (y,z)-plane. These symmetries have been used to reduce the computational work by solving one quarter or one half of the complete problem using appropriate symmetry boundary conditions. In the symmetric flow case a mesh with 576 elements and 5635 nodes has been used. In the asymmetric flow case the mesh contained 1152 elements and 10841 nodes. It has been assumed that the flow will remain symmetric with respect to the above-mentioned planes for all cases considered in this work. This assumption is confirmed by the experimental results described in the section on the validation of the computational model.

At the inflow planes fully developed (parabolic) flow profiles were prescribed. The no-slip boundary condition (zero velocity) was imposed at the walls. At the outlet the normal and both tangential stresses were set to zero. Although this stress-free boundary condition is not completely compatible with fully developed flow, it allows the fluid to leave the computational domain with very little upstream influence. Numerical experiments with different locations of the outflow boundary have shown that the computed solution is affected only over a distance of one element upstream by the imposition of this boundary condition.

The flow field in the outlet tube downstream from $z = 19$ mm, where the flow development has become slow, has been computed with a different method in which use is made of the fact that some terms in the Navier–Stokes equations are very small and can be neglected. Denoting the x,y,z-components of the velocity by u, v and w, respectively, the streamwise diffusion terms u_{zz}, v_{zz} and w_{zz} are deleted. Furthermore, in the z-momentum equation the pressure is replaced by its average over the cross-section. This gives the 'parabolized' Navier–Stokes equations which can be solved as

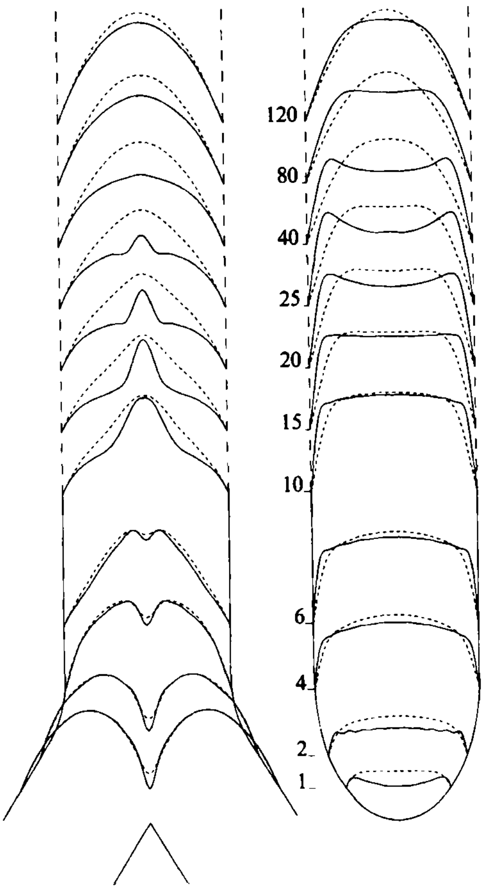

FIGURE 3. Axial velocity profiles in the two planes of symmetry, the (y, z)- and (x, z)-planes, indicated in figure 2. Results for symmetrical inflow and Reynolds numbers 200 (dashed lines) and 600 (continuous lines). All velocities have been made dimensionless by scaling with the corresponding mean axial velocity W. The numbers indicate the downstream distance z. The distances z downstream from the apex are to scale only for $z \leqslant 10$ mm.

a parabolic set with z taking over the role of 'time', using the computed finite-element solution at $z = 19$ mm as an inflow boundary condition. By taking this inflow profile from the finite-element solution at a cross-section located somewhat upstream from the finite-element outflow plane, any undesirable effect of the stress-free boundary condition is avoided. The procedure marches stepwise in the positive z-direction, each time solving a two-dimensional problem by means of an ADI finite-difference method, until the solution has come sufficiently close to the ultimate fully developed state. This approach, of which full details can be found in Krijger *et al.* (1989, 1992), leads to a considerable advantage in computing time.

The computations were done for several values of the Reynolds number, ranging up to 600. The Reynolds number Re is defined by $Re = Wd/\nu$, where W is the cross-sectional average of the axial velocity in the outlet tube, d is the diameter of the outlet tube, and ν is the kinematic viscosity. Measurements with the transcranial Doppler technique have shown that the time-averaged cross-sectional mean of the axial velocity in the basilar artery is approximately 0.45 m s^{-1} (Krijger *et al.* 1991;

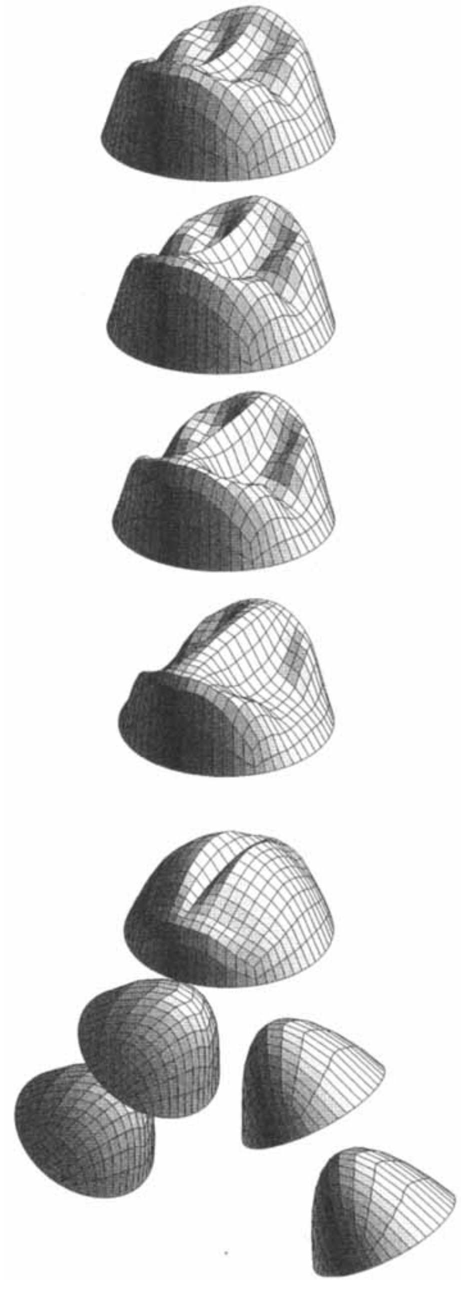

FIGURE 4. Three-dimensional plots of axial velocity profiles for symmetrical inflow at $Re = 600$.

Ravensbergen *et al.* 1995). With blood viscosity $\nu = 3 \times 10^{-6}\ \mathrm{m^2 s^{-1}}$ this implies that Reynolds numbers ranging from 200 to 600 are physiologically realistic.

3. Results

Results will be given for $Re = 200$ and 600, for both symmetrical inflow (inflow ratio $\gamma = 1$) and asymmetrical inflow (inflow ratio $\gamma = 2$). First the case of symmetrical inflow is presented.

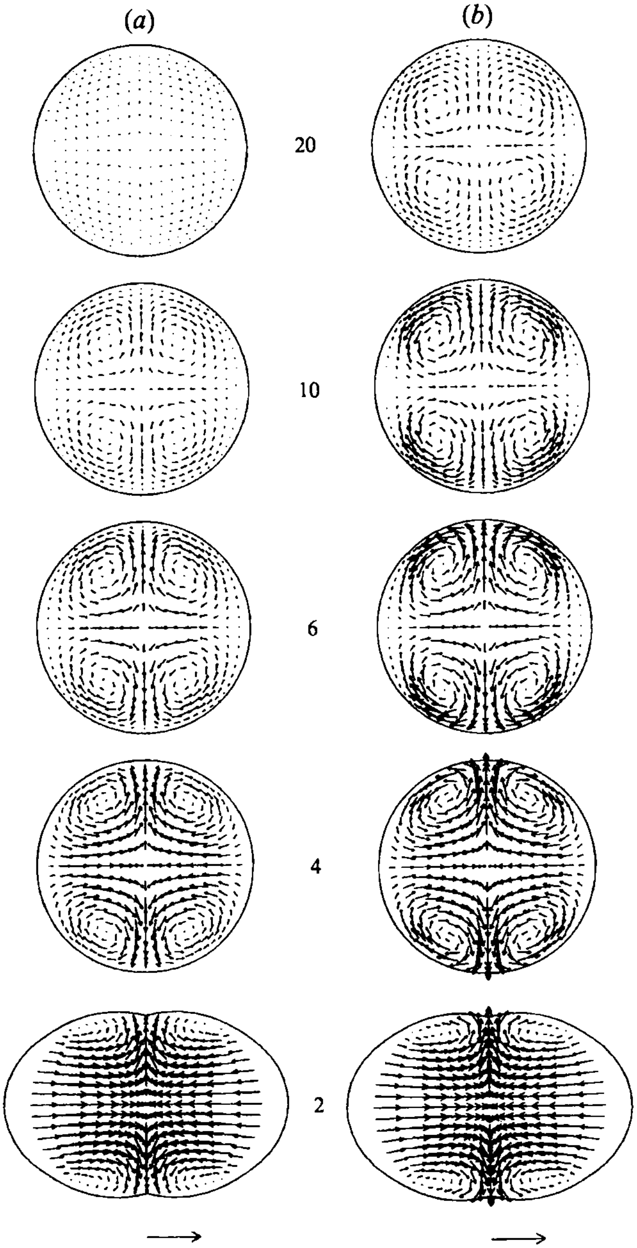

FIGURE 5. Vector plots of the secondary velocities for symmetrical inflow at $Re = 200$ (*a*) and 600 (*b*) at several downstream stations. The mean axial velocity W is indicated by the arrow underneath each column, and the downstream distance z is indicated by the numbers on the plots.

3.1. *Symmetrical inflow*

Profiles of the axial flow velocity, i.e. the z-component w, in the two planes of symmetry (y,z-plane and x,z-plane) at several downstream stations are shown in figure 3. The dashed lines show the results for $Re = 200$. In the plane of the confluence (y,z-plane) a 'double hump' velocity profile appears in the junction region. The two humps merge downstream in the outlet tube and form a profile with one

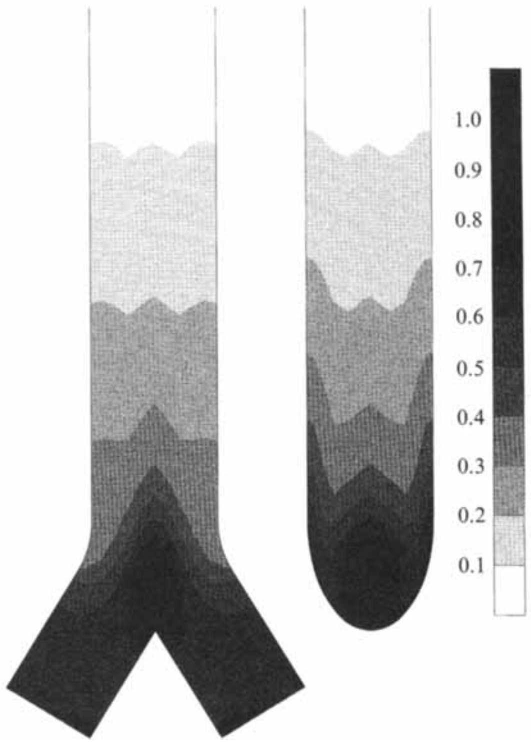

FIGURE 6. Pressure contours for symmetrical inflow at $Re = 600$. The pressure has been nondimensionalized with the reference pressure ρW^2.

central maximum from $z = 10$ mm onwards. From $z = 80$ mm onwards, the flow cannot be distinguished from fully developed flow. Additional phenomena can be observed in the plane perpendicular to the confluence (x, z-plane). Initially the velocity profile is rather flat. Far downstream it develops towards a profile with one maximum. In the entrance region of the outlet tube the velocity gradients near the walls are large. The continuous lines show the results for $Re = 600$. The transition towards full development is much slower than for $Re = 200$. It is noteworthy that in the junction region the flow profiles for $Re = 200$ and 600 show only minor differences, whereas farther downstream noticeable differences occur. For $Re = 600$ the flow profiles in the (y, z)-plane form a pronounced central peak. In the (x, z)-plane the initially flat profile changes into a profile with two maxima which disappear between $z = 80$ and $z = 120$ mm. Three-dimensional plots of complete axial velocity profiles are shown in figure 4 for the case $Re = 600$. The two initial humps collide centrally. Next a sharp ridge develops, which remains visible over a considerable downstream distance.

For a full understanding of the flow phenomena, knowledge of the structure of the secondary flow field and the pressure distribution is indispensible. In figure 5, vector plots of the secondary velocities, i.e. the transverse components u and v, for $Re = 200$ and 600 are shown at five positions between 2 and 20 mm distance from the apex. The secondary flow field consists of four vortices. The strength of these vortices decreases in the downstream direction and the location of their centres changes slightly. The vortices persist very far downstream. It is easy to see that the strength of the secondary flow field varies with the Reynolds number. The effect of the secondary flow field is that the fluid flows in four helical coils and each coil rotates

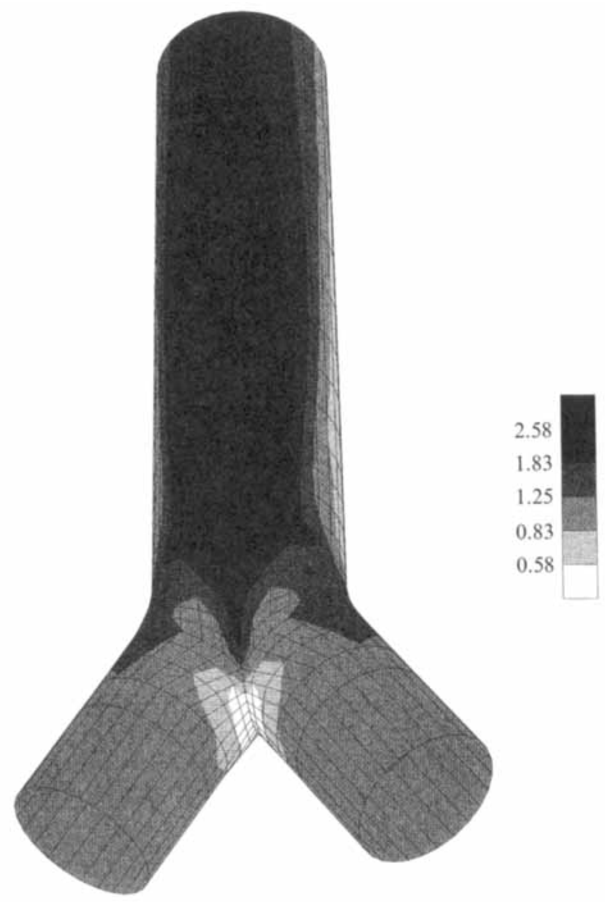

FIGURE 7. Wall shear stress contours for symmetrical inflow at $Re = 600$. The wall shear stress has been nondimensionalized by the standard wall shear stress (see text).

in the opposite direction to neighbouring coils. Figure 6 shows the pressure contours in the two planes of symmetry for symmetrical inflow at $Re = 600$. A pressure maximum is located centrally in the junction region, just downstream from the apex. Hence, in both planes of symmetry, large transverse pressure gradients exist in a small region downstream of the apex. In the plane of the confluence the transverse pressure gradient forces the flow from the inlet tubes to deflect. In the plane perpendicular to the confluence, the pressure gradient causes the fluid to flow outwardly in both directions from the centreline, thus compensating for the fluid being driven inwardly from both sides in the plane of the confluence by the centrifugal effect. As a result, the four vortices in the secondary flow field are created.

The distribution of the wall shear stress for $Re = 600$ is depicted in figure 7. The wall shear stress is defined as the length of the wall shear stress vector that is computed from the derivatives of all three velocity components. It has been made dimensionless by scaling with the standard wall shear stress, i.e. the wall shear stress for Poiseuille flow with the same flux in the outlet channel. As can be seen in figure 7, regions of low wall shear stress can be found around the apex and on both outer walls in the confluence region. High wall shear stresses occur on the wall in the plane

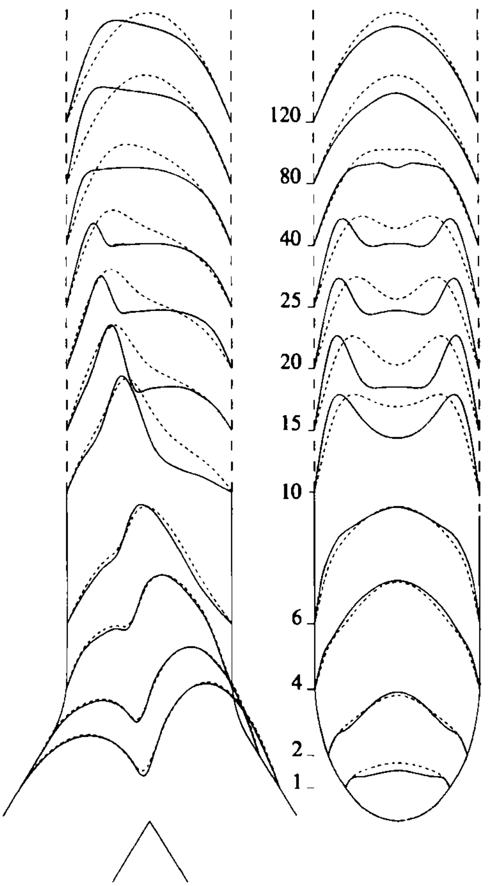

Figure 8. Axial velocity profiles in the two planes of symmetry, the (y,z)- and (x,z)-planes, indicated in figure 2. Results for asymmetrical inflow (with $\gamma = 2$) and Reynolds numbers 200 (dashed lines) and 600 (continuous lines). All velocities have been made dimensionless by scaling with the corresponding mean axial velocity W. The numbers indicate the downstream distance z. The distances z downstream from the apex are to scale only for $z \leqslant 10$ mm.

perpendicular to the confluence plane, coinciding with the regions with steep axial velocity gradients visible in figure 3.

3.2. *Asymmetrical inflow*

Figure 8 shows the flow velocity profiles resulting from asymmetrical inflow with flow ratio $\gamma = 2$, i.e. the flux in one inlet tube is twice the flux in the other. The dashed lines show the results for $Re = 200$. In the plane of the confluence (y,z-plane) the 'double hump' velocity profile in the junction region possesses peaks of unequal height. Farther downstream the highest peak crosses the centreline and it is located on the opposite side from $z = 10$ mm onwards. The asymmetry disappears slowly. The flow phenomena visible in the plane perpendicular to the confluence (x,z-plane) resemble those occurring in the case of symmetrical inflow at $Re = 600$. The continuous lines show the results for asymmetric inflow at $Re = 600$. Initially, in the junction region, the profiles are quite similar to those for $Re = 200$, but farther downstream marked differences develop. For $Re = 600$ the transition zone is much longer and a fully developed flow velocity profile has not yet established itself at $z = 120$ mm. Note

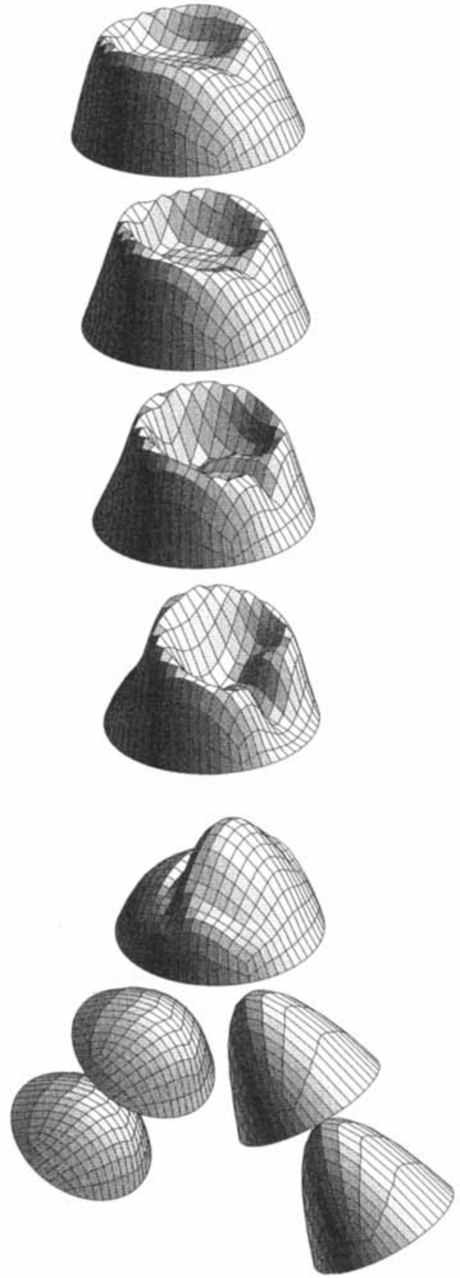

FIGURE 9. Three-dimensional plots of axial velocity profiles for asymmetrical inflow (with $\gamma = 2$) at $Re = 600$.

that, up to $z = 15$ mm in the (y, z)-plane, the trajectory of the highest peak appears to be almost independent of the Reynolds number. Figure 9 shows three-dimensional plots of the axial velocities at $Re = 600$. In the junction region the highest peak dominates the other peak, whereupon a C-shaped maximum with a remarkable sharp ridge develops. The cavity within the 'C' fills up slowly as the flow approaches full development.

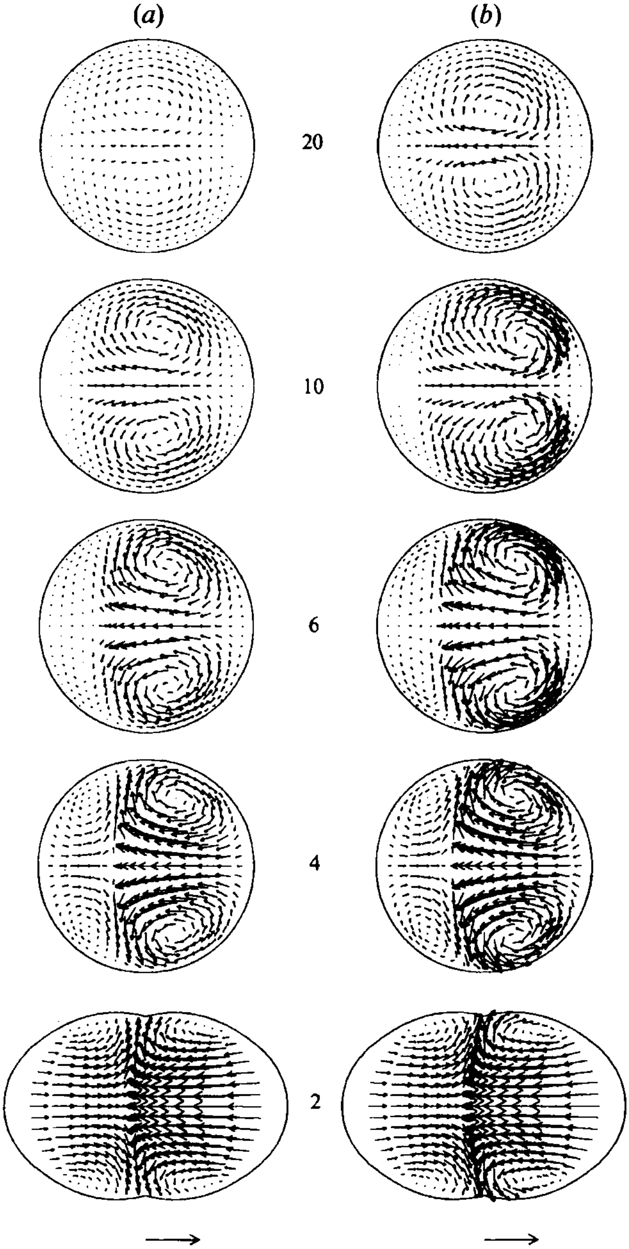

FIGURE 10. Vector plots of the secondary velocities for asymmetrical inflow (with $\gamma = 2$) at $Re = 200$ (*a*) and 600 (*b*) at several downstream stations. The mean axial velocity W is indicated by the arrow underneath each column, and the downstream distance z is indicated by the numbers on the plots.

The secondary velocities for asymmetrical inflow at $Re = 200$ and 600 are presented in figure 10 for five positions between 2 and 20 mm distance from the apex. Again four vortices are found. However, the two vortices on the side of the largest inflow are stronger than the other two. The strongest vortices occupy a growing area and decay more slowly. Figure 11 shows the pressure contours for the case $Re = 600$. As in the symmetrical flow case, a region of high pressure is located just downstream from the

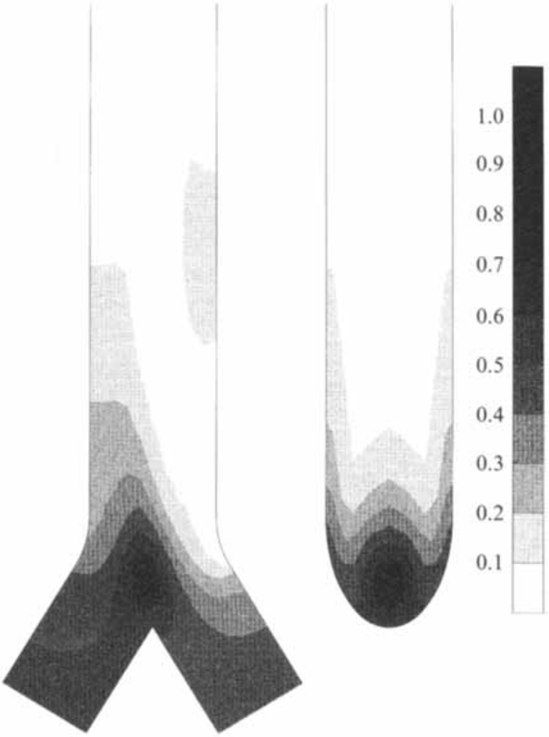

FIGURE 11. Pressure contours for asymmetrical inflow (with $\gamma = 2$) at $Re = 600$. The pressure has been nondimensionalized with the reference pressure ρW^2.

apex. The transverse pressure gradients in the plane of the confluence are unequal now. Notwithstanding the fact that the pressure gradient is larger on the right-hand side, the flow on this side, which possesses the highest velocities, is less deflected than the flow on the other side. As a result, the highest velocities cross the centreline of the outlet tube. Furthermore, a local pressure maximum is observed downstream near the right-hand wall of the outlet tube. However, a detailed examination of the velocities in this region did not reveal any local backflow phenomena.

The distribution of the wall shear stress for asymmetrical inflow at $Re = 600$ is shown in figure 12. Near the apex and on both lateral walls a region of low wall shear stress is present. On the lateral wall on the side of the largest inflow the region of low wall shear stress is much larger (and the stress values are much lower) than on the opposite wall. High wall shear stresses occur on the wall in the plane perpendicular to the confluence.

4. Validation of the computational model

4.1. *Description of the validation model*

The computational model is validated by hydrodynamical experiments under steady flow conditions in a symmetrical model consisting of tubes with a rectangular cross-section. Figures 13(*a*) and 13(*b*) show the model geometry, which is fully characterized by the branching angle, the height and width of the cross-sections and the radius of curvature of the tube outer walls at the junction. These characteristics of the validation model are comparable with those of the model with the circular tubes.

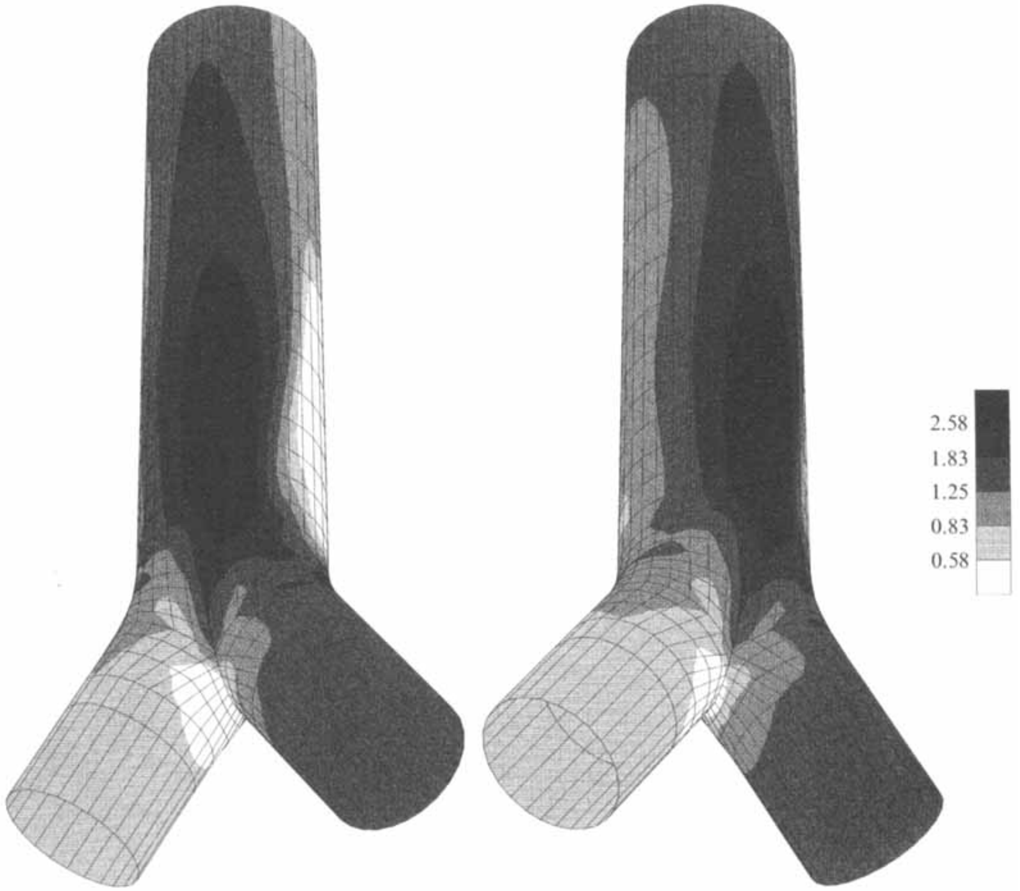

FIGURE 12. Two views of the wall shear stress contours for asymmetrical inflow (with $\gamma = 2$) at $Re = 600$. The wall shear stress has been nondimensionalized by the standard wall shear stress (see text).

Rectangular tubes have the advantage that the manufacturing of a Perspex model is less complicated and that the geometries of the experimental and the computational model can be made identical. Also, the measurements with the laser Doppler technique are not compromised by refraction problems at the wall of the model. For the validation, the axial velocity component (w) is measured using laser Doppler velocimetry, and compared with computed velocities in the two symmetry planes at locations where the flow is most complicated. Symmetrical inflow as well as asymmetrical inflow are investigated, both for several Reynolds numbers. Furthermore, the results of dye experiments are compared with the computed streamlines.

In the experimental Perspex model the vertebral arteries are represented by two identical tubes with rectangular cross-section of 3 × 4 mm and a length of 70 mm. The inlet tubes meet symmetrically with an angle of 63° and form a single outlet tube with a cross-section of 4 × 5 mm and a length of 200 mm, representing the basilar artery. The ratio of the total cross-sectional luminal area of the vertebral arteries and of the basilar artery is 1.2. In the junction region the outer walls are curved, the circular arcs having a radius of 1.5 mm. The computational mesh used is depicted in figure 13(c), and the same numerical solution technique has been used as for the circular tube model.

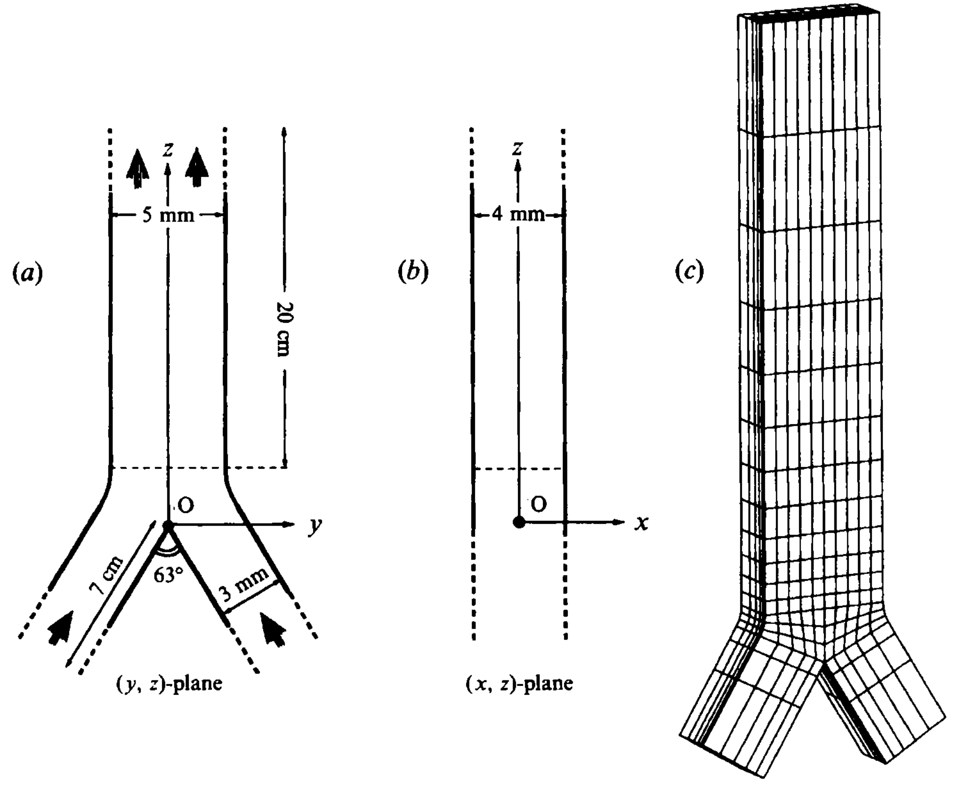

FIGURE 13. (*a*, *b*) Definition sketches of the validation model. (*c*) Finite-element discretization of the validation model.

4.2. *The experimental set-up*

The Perspex model was mounted on a support allowing three degrees of freedom in translation. The measurements were made at several locations in the outlet tube. Most measurements were made in the region were the flow was known from previous research to be very complicated. A steady flow was provided with water as the fluid. Two flowmeters (Brooks SHO-RATE purgemeters 1357 with needle valves and with an accuracy higher than 97%) were placed in the two supply hoses to control the incoming flow rates. The temperature was kept under control throughout the experiments.

A computer-controlled differential laser Doppler velocimeter was used in a forward scattering mode. A helium–neon laser (Optilas LHRR-0100) produced a laser beam with $\lambda = 633$ nm at 1 mW. A prism cube beamsplitter and several prisms (CVI) on adjustable mounting systems produced two parallel laser beams of equal intensity and with optical path lengths which did not exceed the coherence length of the laser. A lens focused the laser beams ($f = 25$ mm) to form an intersecting sampling volume that was approximately ellipsoidal with a length of 90 μm and a diameter of 25 μm. Within the sampling volume fringes were established by interference. Polystyrene microspheres in dilute suspensions were used as laser scattering particles. Light scattered by these particles traversing the fringes was collected by a photodetector (Spindler & Hoyer E2VUV), amplified and filtered (HP 462A amplifier; Krohnhite 3100 band-pass filter) and fed into a computer. An AD-converter card digitized the electrical signal and the individual Doppler bursts were selected automatically and analysed by a software package which calculated the average velocity of 100 Doppler bursts for each local velocity measurement (Nijhof, Uijttewaal & Heethaar 1994).

In addition, experiments with dye injection were performed to obtain visual information on the flow phenomena. Streamlines were generated at several locations in the two inlet tubes by injecting dark blue and dark red ink in the separate tubes. Injection was performed through a needle with an internal diameter of 0.05 mm at the entrance of the inlet tubes in order to keep the confluence free of disturbances.

4.3. *Comparison of numerical and experimental results*

Measurements and computations were performed for $Re = 200$, 400 and 600 (based on $d = 5$ mm) with symmetrical inflow (flow ratio $\gamma = 1$) and asymmetrical inflow (flow ratio $\gamma = 2$). The flow velocities were measured in the two planes of symmetry, indicated in figure 13 as the (y,z)-plane and (x,z)-plane. Figure 14 shows the axial velocity profiles for symmetric inflow at $Re = 400$ and asymmetric inflow at $Re = 400$ and $Re = 600$. The circles denote the measured values and the lines the corresponding computations. The numerically predicted flow velocities are seen to agree very well with the measurements. The same holds for the results not shown here. A minor imperfection occurs in figure 14(*c*) (asymmetric inflow, $Re = 600$) where the largest inflow in the experiment turned out to be not completely developed, whereas in the computations fully developed flow at both inlets of the model is always assumed. This shortcoming in the experiments arises from the fact that for asymmetric inflow at higher *Re*-values the flow in the inlet tubes depends quite strongly on the way the supply hoses are connected to the Perspex model. In particular, owing to the set-up of the flow circuit, curves in the flexible supply hoses could not be avoided completely.

The axial velocity profiles shown in figure 14 are essentially the same as those for the circular tube model. In addition, the computed secondary flows (not shown here) are also very similar to those in the circular tube model. Secondary velocity vector plots, computed for an almost identical junction model composed of tubes with rectangular cross-section, have been presented by Krijger *et al.* (1992) for both symmetric and asymmetric flow at $Re = 250$.

The visualization of streamlines by the dye experiment and the computed streamlines of two of the four helices for $Re = 600$ is given in figure 15. The computed streamlines agree very well with the ink lines. The streamlines swirl slowly in a direction corresponding to the four-vortex secondary flow pattern. In the symmetric case the fluid remains on its own side, but in the asymmetric case there is an exchange of fluid across the plane perpendicular to the plane of the confluence.

5. Discussion

Summarizing the main results, it can be concluded that the flow in the vertebro-basilar junction model is highly three-dimensional. As a consequence of the deflection of the two inlet flows in the junction region a strong secondary flow field is created which persists far downstream. The transverse velocities show a distinctive four-vortex pattern. No essential differences have been found between the flow phenomena occurring in the circular tube model and those in the rectangular tube model.

In the case of symmetric inflow, the fluid in the vertebro-basilar junction model flows in four 'compartments' and the fluid in one compartment never mixes with fluid

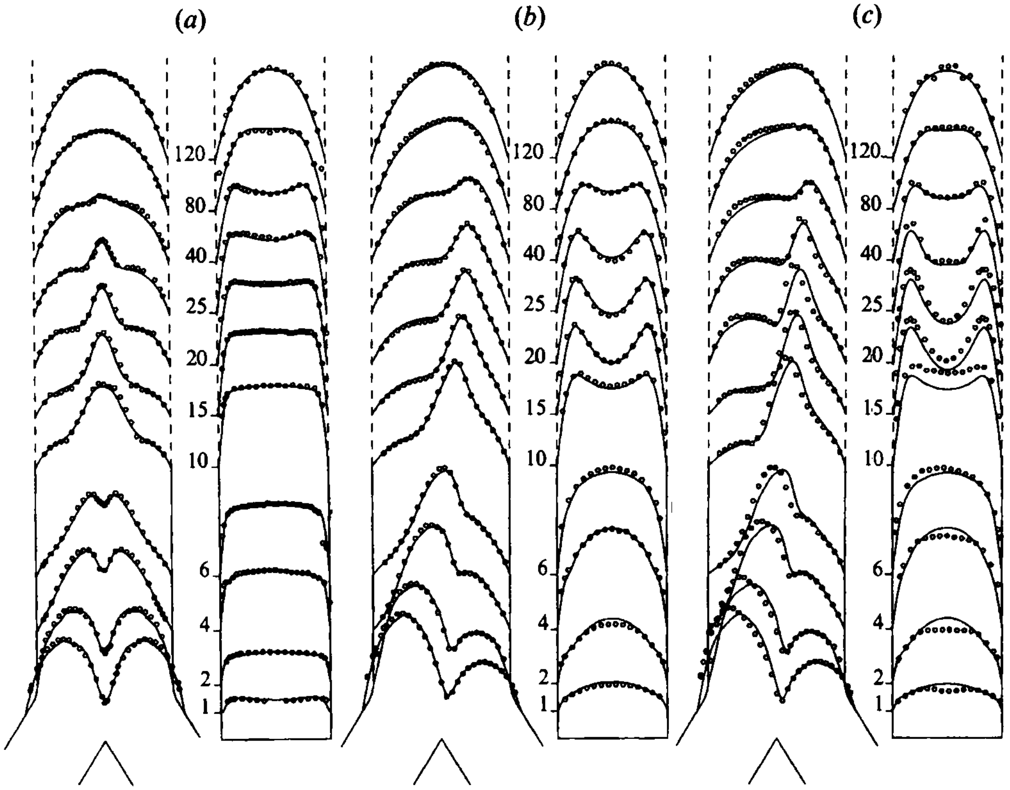

FIGURE 14. Computed (lines) and measured (circles) axial velocity profiles in the two planes of symmetry, (y,z)- and (x,z)-planes, indicated in figure 13. (*a*) Results for symmetrical inflow at $Re = 600$. (*b*) Results for asymmetrical inflow (with $\gamma = 2$) at $Re = 400$. (*c*) Results for asymmetrical inflow (with $\gamma = 2$) at $Re = 600$. All velocities have been made dimensionless by scaling with the corresponding mean axial velocity W. The numbers indicate the downstream distance z. The distances z downstream from the apex are to scale only for $z \leqslant 10$ mm.

from other compartments. This is in accordance with McDonald & Potter (1951), who showed experimentally that there was no mixing between the flow from the left and the right vertebral arteries in the basilar artery of young rabbits with vertebrals of equal diameter.

Some flow phenomena observed in our work were noted earlier by Schroter & Sudlow (1969). As already mentioned in the introduction, they studied inspirational and expirational air flow in symmetric models of the human respiratory system for Reynolds numbers in the same range as used here. In expiration, merging flows occur in the airways which are comparable to the flow conditions considered in the present paper. The results of Schroter & Sudlow are mainly qualitative, and our study provides additional quantitative information (for both symmetric and asymmetric inflow) on the three-dimensional flow field, the strength of the secondary flow field, the pressure distribution and the distribution of the wall shear stress. Moreover, a comparison is made between numerical and experimental results.

Pedley (1977), referring to the results of Schroter & Sudlow (1969), noticed that secondary motions cause the fluid just downstream of the apex, which has a low flow velocity, to be swept out away from the plane of the confluence. So, the fluid with the highest flow velocity accumulates in the centre, developing a single central maximum

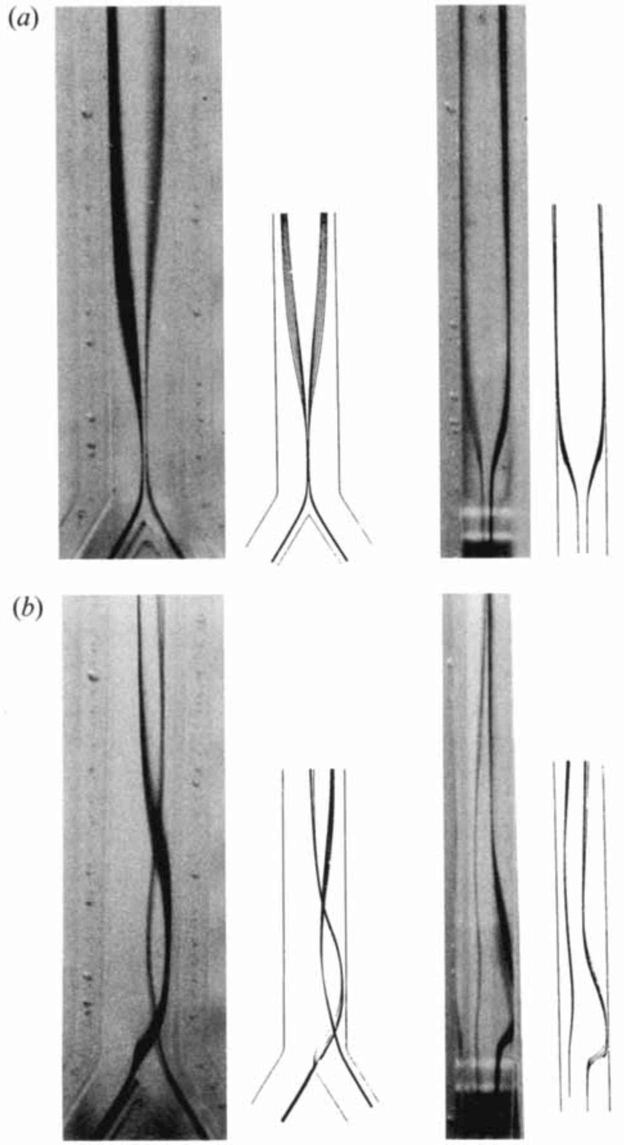

FIGURE 15. Comparison between flow visualization with ink lines in the experimental model and computed streamlines starting at comparable locations. (*a*) Symmetric inflow at $Re = 600$. (*b*) Asymmetric inflow ($\gamma = 2$) at $Re = 600$.

in the axial velocity profile. Further downstream the secondary motions also cause the fluid in the centre of the model to be swept out away from the confluence plane, but as this fluid has the highest velocities, two new maxima develop in the plane perpendicular to the confluence. Furthermore, over a considerable distance in the outlet tube, the axial velocity profiles remain rather flat. This is apparently due to the mixing effect of the complicated pattern of secondary velocities on the axial velocities. This explanation of some of the phenomena occurring in merging flows is confirmed by the findings reported in the present paper.

Secondary velocities are often associated with flow in curved tubes, a subject which has attracted much attention in the literature (Berger, Talbot & Yao 1983). For fully

	$\gamma = 1$			$\gamma = 2$		
	$Re = 200$	$Re = 400$	$Re = 600$	$Re = 200$	$Re = 400$	$Re = 600$
1%	65.84	148.14	225.69	96.56	208.98	312.60
2%	54.38	125.04	191.81	83.77	182.83	273.48
3%	48.30	111.79	170.44	75.96	166.09	248.39

TABLE 1. Inlet lengths (mm) with tolerances 1, 2 and 3 % for the circular tube model. Results for symmetrical ($\gamma = 1$) and asymmetrical ($\gamma = 2$) inflow, for $Re = 200$, 400 and 600.

developed flow in long curved tubes a balance has been reached between centrifugal forces (which accelerate the fluid in the transverse direction) and viscous forces (which slow down the fluid). The Dean number characterizes this balance and indicates the strength of the secondary flow field for fully developed flow in a curved tube. Owing to the short and acute bends in the junction model of the present study, the secondary flow field cannot develop fully. Therefore, a balance between inertial and viscous forces cannot be reached, and the Dean number is not a measure of the strength of the secondary flow field. In the present study, the secondary flow velocities appear to depend on the magnitude of the transverse pressure gradients. These transverse pressure gradients are associated with the change of direction of the flow, which, in turn, depends on the angle of confluence, and not on Re. An analogous argument for entry flow into a curved tube can be found in Berger *et al.* (1983).

It takes a certain length, the inlet length, for fully developed Poiseuille flow to establish itself in the outlet tube. Strictly speaking, since the fully developed state is reached asymptotically, this length is infinite. For practical purposes it is convenient to define the inlet length as the length needed for the flow to become close to the fully developed state. In the classical entry flow problem, in which the fluid enters a straight tube with a flat axial velocity profile, an often applied criterion for the inlet length is that the centreline velocity has reached a value equal to 99% of the fully developed value. In the present context a more general criterion is needed. The inlet length L is defined here as the smallest value of the axial coordinate z for which the maximum value over the cross-section of the difference $|w(x,y,z)-w(x,y,\infty)|$ is equal to n% of the fully developed centerline velocity $w(0,0,\infty)$. This definition has been introduced by Krijger *et al.* (1992). For the classical entry flow problem it reduces to the classical one. The results presented in table 1 show that L in the asymmetric case is larger than in the symmetric case. Moreover, in both cases, L exceeds the length of the real basilar artery considerably, which means that the flow branching at the end of the basilar artery will be heavily influenced by the secondary flow effects created by the vertebro-basilar junction. The different values of L, computed for $n = 1$, 2 or 3, illustrate the rate at which the flow reaches full development.

Provided the Reynolds number is sufficiently large, the inlet length is almost proportional to Re: $L/d = \beta Re$. For the classical axisymmetric entry flow problem the most accurate value of the constant of proportionality β, based on a 99% tolerance ($n = 1$), is 0.056. This value was computed by Friedman, Gillis & Liron (1968), who solved the full Navier–Stokes equations. For symmetric junction flow ($\gamma = 1$) in the circular tube model the value $\beta = 0.075$ has been found here, and for asymmetric flow (with $\gamma = 2$) β becomes 0.104. Values of β have also been computed for the rectangular tube model. Using the hydraulic diameter ($d = 4.444$ mm) in the definition of Re, the result is $\beta = 0.075$ for the symmetric flow case and $\beta = 0.121$ for the asymmetric case with $\gamma = 2$. It can be concluded that for symmetric

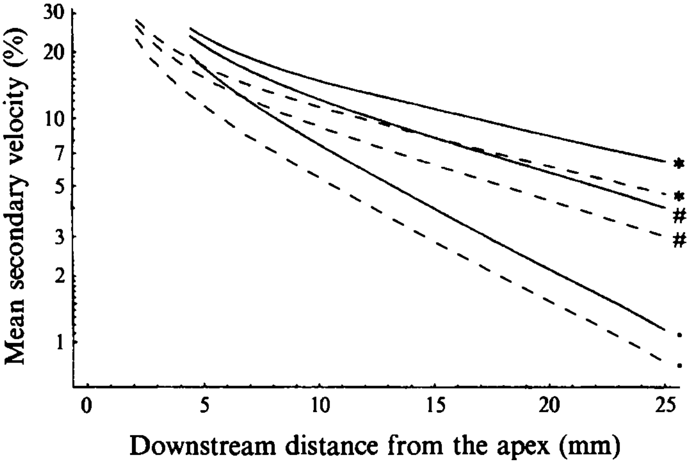

FIGURE 16. Cross-sectional mean of the secondary velocities in the outlet channel (expressed as a percentage of the mean axial velocity) as a function of the distance z from the apex for symmetrical inflow at Re = 200(o), 400(#) and 600(*) on a logarithmic scale. The dashed lines indicate the results for the rectangular tube model and the continuous lines those for the circular tube model.

inflow the inlet length in the basilar artery is somewhat larger than the classical inlet length. However, for asymmetric flow the classical value underestimates the inlet length considerably.

The good agreement between measured and computed velocities for a range of flows in the rectangular tube model justifies the belief that the computational results for flows in the circular tube model are reliable. Moreover, the flow phenomena in both types of junction model turn out to be essentially the same. Apparently, the corner regions of nearly stagnant flow in the rectangular tube model do not contribute much to the overall flow phenomena. In addition to the agreement between the inlet parameters β noted in the preceding paragraph, another quantitative comparison between the results from the two models can be made by comparing the cross-sectional mean of the secondary velocities. Figure 16 shows the mean secondary velocities in the outlet tube (on a logarithmic scale, and expressed as a percentage of the mean axial velocity) as a function of the distance from the apex for symmetrical inflow at various values of Re. The continuous lines show the results for the circular tube model and the dashed lines those for the rectangular tube model. Note that the graphs start at different axial positions for each model, since the length of the junction region is larger for the circular tube model compared with the rectangular tube model. As can be seen, the initial mean secondary velocities as well as the decay rates differ only slightly between the two models.

Our experiments and computations were based on some assumptions: (i) rigid tube walls, (ii) Newtonian fluid behaviour and (iii) steady flow. Although vessel compliance is important with regard to wave propagation (McDonald 1974; Pedley 1980), its effect on the global flow field will be very small. In the real basilar artery relative diameter changes during the cardiac cycle are less than 5% (Ku & Liepsch 1986). Hence, the flow will be influenced only close to the tube wall, with probably an effect on the magnitude of the wall shear stress. The assumption that blood behaves as a Newtonian fluid is a very common one when considering blood flow in the larger arteries (Xu, Collins & Jones 1992). The particles in the blood, i.e. the blood cells, as well as the particles in the experimental fluid, i.e. the polystyrene microspheres, have much smaller dimensions than the vessels or the tubes in the model. The difference is about threehundred-fold.

The assumption of steady flow is not without drawbacks since it ignores the important effects of flow acceleration and deceleration. A representative parameter for the influence of the frequency on the balance between inertial and viscous forces is the Womersley parameter $\alpha = R(2\pi f/\nu)^{1/2}$. This parameter is determined by the radius (R) of the vessel, the frequency (f) and the kinematic viscosity (ν). For the flow in the basilar artery the Womersley parameter is about 2.1 which is small enough to assume that with respect to the frequency the effects of unsteadiness will be moderately small. Furthermore, the amplitude of the flow fluctuation in the human basilar artery is not very large. For the cerebral circulation this fluctuation is often expressed by the pulsatility index after Gosling, which is defined as the difference between the maximum and minimum velocities divided by the mean flow velocity over the cardiac cycle. For the basilar artery this pulsatility index is less than one (Ravensbergen *et al.* 1995), which is relatively small. In previous work (Krijger *et al.* 1991) a two-dimensional model of pulsatile flow in the basilar artery led to results which were largely similar to those for the steady case. The largest differences occurred during the phase of strongly decelerating flow.

It is generally accepted that hemodynamic forces are associated with atherogenesis. There are various reasons to think that the wall shear stress is an important factor in the development of atherosclerosis. Anatomical data suggest that the sites on the vessel walls exposed to low or oscillating wall shear stress are highly susceptible to atherosclerosis. The basilar artery is often affected with this disease. A location with a striking amount of atherosclerotic plaques is the apex. Of the 85 preparations studied morphologically, 43 had an atherosclerotic plaque at the apex, by far the highest percentage in comparison with all other locations. As can be seen in figures 7 and 12, the wall shear stress is rather low at the apex of the vertebro-basilar junction, for symmetrical as well as for asymmetrical inflow. In contrast, the apex of a bifurcation, which is known to be a location with relatively high wall shear stresses, is often spared (Kjearness *et al.* 1981; Zarins *et al.* 1983; Ku *et al.* 1985).

This research was supported by the Netherlands Organization for Scientific Research, NWO.

REFERENCES

BERGER, S. A., TALBOT, L. & YAO, L. S. 1983 Flow in curved pipes. *Ann. Rev. Fluid Mech.* **15**, 461–512.

CARO, C. G., PEDLEY, T. J., SCHROTER, R. C. & SEED, W. A. 1978 *The Mechanics of the Circulation.* Oxford University Press.

CUVELIER, C., SEGAL, A. & VAN STEENHOVEN, A. A. 1986 *Finite Element Methods and Navier-Stokes Equations.* Dordrecht: D. Reidel.

FRIEDMANN, M., GILLIS, J. & LIRON, N. 1968 Laminar flow in a pipe at low and moderate Reynolds numbers. *Appl. Sci. Res.* **19**, 426–438.

HAYASHI, K., NUNOMORA, M., NAIKI, T. & ABE, H. 1992 LDA studies of flow characteristics in a vertebrobasilar arterial junction model. In *Proc. 7th Intl Conf. on Biomedical Engineering, Singapore, December 1992*, pp. 61–64.

KJEARNES, M., SVINDLAND, A., WALLOE, L. & WILLE, O. 1981 Localization of early atherosclerotic lesions in an arterial bifurcation in humans. *Acta Path. Microbiol. Scand.* A **89**, 35–40.

KRIJGER, J. K. B., HEETHAAR, R. M., HILLEN, B., HOOGSTRATEN, H. W. & RAVENSBERGEN, J. 1992 Computation of steady three-dimensional flow in a model of the basilar artery. *J. Biomech.* **25**, 1451–1465.

KRIJGER, J. K. B., HILLEN, B. & HOOGSTRATEN, H. W. 1989 Mathematical models of the flow in the basilar artery. *J. Biomech.* **22**, 1193–1202.

KRIJGER, J. K. B., HILLEN, B. & HOOGSTRATEN, H. W. 1991 A two-dimensional model of pulsating flow in the basilar artery. *Z. Angew. Math. Phys.* **42**, 649–662.

KRIJGER, J. K. B., HILLEN, B., HOOGSTRATEN, H. W. & VAN DEN RAADT, M. P. M. G. 1990 Steady two-dimensional merging flow from two channels into a single channel. *Appl. Sci. Res.* **47**, 233–246.

KU, D. N., GIDDENS, D. P., ZARINS, C. K. & GLAGOV, S. 1985 Pulsatile flow and atherosclerosis in the human carotid bifurcation. *Arteriosclerosis* **5**, 293–302.

KU, D. N. & LIEPSCH, D. W. 1986 The effects of non-Newtonian viscoelasticity and wall elasticity on flow at 90 degrees bifurcation. *Biorheology* **23**, 359–370.

MCDONALD, D. A. 1974 *Blood Flow in Arteries.* London, Arnold.

MCDONALD, D. A. & POTTER, J. M. 1951 The distribution of blood to the brain. *J. Physiol.* **114**, 356–371.

NIJHOF, E. J., UIJTTEWAAL, W. S. J. & HEETHAAR, R. M. 1994 A laser Doppler system for measuring distributions of blood particles in narrow flow channels. *IEEE Trans. Instrum. Meas.* **43**, 430–435.

PEDLEY, T. J. 1977 Pulmonary fluid dynamics. *Ann. Rev. Fluid Mech.* **9**, 229–274.

PEDLEY, T. J. 1980 *The Fluid Mechanics of Large Blood Vessels.* Cambridge University Press.

RAVENSBERGEN, J., TARNAWSKI, M., VRIENS, E. M., HILLEN, B., CARO, C. G. & VAN HUFFELEN, A. C. 1995 New facilities to perform in vivo flow velocity measurements in the basilar artery. *Neuroradiology* (to appear)

SCHROTER, R. C. & SUDLOW, M. F. 1969 Flow patterns in models of the human bronchial airways. *Respiration Physiol.* **7**, 341–355.

SEGAL, A. 1993 *Sepran User Manual.* Leidschendam, The Netherlands: Ingenieursburo SEPRA.

VAN DE VOSSE, F. N., VAN STEENHOVEN, A. A., SEGAL, A. & JANSSEN, J. D. 1989 A finite element analysis of the steady laminar entrance flow in a 90° curved tube. *Intl J. Numer. Meth. Fluids* **9**, 275–287.

XU, X. Y., COLLINS, M. W. & JONES, C. J. H. 1992 Flow studies in canine artery bifurcations using a numerical simulation method. *ASME J. Biomech. Engng Trans.* **114**, 504–511.

ZARINS, C. K., GIDDENS D. P., BHARADVAJ, B. K., SOTTIURAI, V. S., MABON, R. F. & GLAGOV, S. 1983 Carotid bifurcation: quantitative correlation of plaque localisation with flow velocity profiles and wall shear stress. *Circulation Res.* **53**, 502–514.